Eur. Phys. J. B **19**, 225–239 (2001)

THE EUROPEAN PHYSICAL JOURNAL B

EDP Sciences

Stabilisation of fcc cobalt layers by 0.4 nm thick manganese layers in Co/Mn superlattices

A. Michel[1,a], V. Pierron-Bohnes[1], J.P. Jay[1,b], P. Panissod[1], S. Lefebvre[2], M. Bessière[2], H.E. Fischer[2], and G. Van Tendeloo[3]

[1] IPCMS, GEMM[c], 23, rue du Loess, 67037 Strasbourg, France
[2] LURE, Bâtiment 209 D, Centre Universitaire Paris-Sud, 91898 Orsay Cedex, France
[3] EMAT-University of Antwerp, Groenenborgerlaan 171, 2020 Antwerpen, Belgium

Received 27 October 1999 and Received in final form 29 May 2000

Abstract. Epitaxial Co/Mn multilayers (0.75 to 6 nm Co, 0.4 nm Mn layer thickness) have been grown on mica substrates covered by a (0002) Ru buffer layer. The structural properties of these layers have been studied using X-ray diffraction, nuclear magnetic resonance (NMR), and high resolution transmission electron microscopy (HRTEM). The Co layers, grown as face centred cubic (fcc), were found to be stabilised by the very thin Mn layers. Data obtained using X-ray diffraction and NMR were analysed and found to be in good agreement, while Monte-Carlo simulations were used to interpret the data and calculate the expected diffracted intensity and NMR spectra. The HRTEM data show that the Mn layers give rise to a large strain contrast extending, in the growth direction, over a distance which exceeds the thickness of the Mn layers. The superlattices could be described as having an fcc structure containing randomly located stacking faults with varying densities. The results verify the presence of a dominant, almost perfect phase of fcc stacking, and of a faulted hcp phase, while the number of defects increases with the Co layer thickness.

PACS. 61.10.-i X-ray diffraction and scattering – 61.16.-d Electron, ion, and scanning probe microscopy – 61.50.-f Crystalline state – 64.60.My Metastable phases

1 Introduction

During the last ten years, a great interest has been given by the scientific community to metallic multilayers as possible media for high density magnetic recording and magnetic sensors. Generally, they result from the stacking of two different types of layers: a layer of ferromagnetic material, such as cobalt, and a layer of either a non-magnetic or an antiferromagnetic material. The interesting physical properties are the result of the coupling between the magnetic layers through the spacer layers [1–8]. The structural properties of these systems are important because they determine the magnetic properties. The characteristics of the superlattice, such as the period, the number and thickness of the layers, are important in order to understand and predict the magnetic behaviour of these systems. The crystal structure within the magnetic layers, their correlation length and their thickness govern the magnetic anisotropy that gives rise to a perpendicular magnetisation, necessary for a high density recording medium. Moreover, the interface morphology, roughness and interdiffusion influences greatly the coupling between the magnetic layers and thus the magnetoresistance [9–12].

The Co/Mn superlattice is a good example of a multilayer system with a ferromagnetic and an antiferromagnetic element having large magnetic moments. Indeed, manganese is antiferromagnetic in some crystallographic phases (compressed γ phase). Additionally, for thin Mn layers, evidence of an antiferromagnetic coupling [13–15] was found, in contrast to more complicated coupling observed in other conditions [16–18]. In our previous studies of this system [19,20], we examined a series of samples (Series I hereafter) having a constant Co thickness (nominally 3 nm) and a varying Mn thickness (nominally between 0.4 and 3 nm).

The Series I samples were grown on a mica substrate on which a Ru buffer layer was deposited. We have shown [19–21] that this buffer layer grows with an hcp structure having the c-axis parallel to the growth direction, and the cobalt and manganese layers grow epitaxially on this buffer layer. Reflection High Energy Electron Diffraction (RHEED) observations during the growth, X-ray

[a] *Present address:* LMP, UMR 6630, SP2MI, boulevard Pierre et Marie Curie, Téléport 2, BP 30179, 86962 Futuroscope Cedex, France.
e-mail: Anny.S.Michel@univ-poitiers.fr
[b] *Present address:* Laboratoire de Magnétisme de Bretagne, CNRS UPRES-A 6135, Université de Bretagne Occidentale, 6 avenue Le Gorgeu, BP 809, 29285 Brest, France.
[c] UM0046 CNRS-ULP-ECPM.

diffraction and Ferromagnetic Resonance (FMR) studies on the grown samples have shown that the structure of both Co and Mn layers changes at a Mn nominal thickness of 1.6 nm [19]. For thinner Mn layers, both Co and Mn adopt an fcc metastable structure (bulk Co is fcc at $T > 693$ K and bulk Mn is fcc at $T > 1373$ K) with the Co layers having few stacking faults [21]. The growth axis is then a [111] axis of the fcc structure, the in-plane $[1\bar{1}0]$ and $[\bar{1}\bar{1}2]$ directions are respectively parallel to the $[11\bar{2}0]$ and $[10\bar{1}0]$ directions of the hcp Ru buffer.

For thicker Mn layers, additional streaks appear in the RHEED patterns corresponding to a three times larger period in the $[10\bar{1}0]$ hcp direction. The intensity variations along the streaks, due to a non planar growth, have been described as a 3D diffraction [19] corresponding to the $MgCu_2$-type Laves phase structure, very close to the bulk α-Mn phase, and stable at room temperature. In fact, when the growth of these samples is completed (*i.e.* when the Mn is covered by Co), the structure of the Mn layers is different [20]: X-ray diffraction and transmission electron microscopy have shown that thick Mn layers consist of small, misoriented, and deformed fcc and α-phase grains. At the same time, the cobalt recovers [21] its bulk, stable hcp phase, with its axes parallel to those of the ruthenium, but with a large number of stacking faults, as observed using asymmetric X-ray diffraction.

The current study focuses on the stabilisation of the fcc Co phase by a very thin Mn layer. For this purpose, another set of samples (Series II) having constant Mn thickness (0.4 nm nominal) and a varying Co thickness was prepared. The Co layers had a thickness of 0.75, 1.2, 1.5, 3.0, 4.5, and 6.0 nm (labelled sample 1 to sample 6), while the number of bilayers was chosen appropriately in order to maintain a total superlattice thickness of about 75 nm. An additional sample, having 30 bilayers, was grown for the studies at the LURE synchrotron. The nominal layer thickness for this sample were 0.6 nm and 2.0 nm for Mn and Co, respectively.

The epitaxial growth of the Series II samples, following the same procedure as for the Series I samples, has been performed under UHV (base pressure of $\sim 5 \times 10^{-11}$ torr, growth pressure $\sim 5 \times 10^{-10}$ torr). The samples were grown on single-crystal muscovite mica substrates after an initial deposition, at 850 K, of a 15 nm Ru buffer layer to further improve the crystalline quality. A seed layer of Mn, having a thickness of 0.6 nm, was necessary for the good epitaxial growth of Co, as Co does not wet Ru as well as Mn [22,23]. The layer thickness was monitored by a quartz micro balance and the growth was performed at 260 K, *i.e.* the chamber temperature maintained by the cryogenic shields. At higher temperatures, the manganese diffuses rapidly into the cobalt or the ruthenium layers. The multilayers were covered by a 5 nm capping Ru layer to prevent any oxidisation.

The samples were studied using different, complementary techniques: X-ray diffraction, in symmetric and asymmetric geometries (as presented in Sect. 2) using both in-house and synchrotron facilities, Nuclear Magnetic Resonance (Sect. 3), as well as Transmission Electron Microscopy (Sect. 4). Each section consists of a short description of the employed method and equipment, a reference to the acquired data and a preliminary, yet complete, analysis of these data. The last part (Sect. 5) is dedicated to the detailed discussion of the results.

In the following sections, the thickness is given as the nominal thickness, unless otherwise specified.

2 X-ray diffraction

2.1 Experimental details

Two diffractometers were used in the laboratory: a Philips HRD three circle diffractometer for high resolution diffraction, and a Siemens D500 two axes diffractometer, when the need for high intensity was essential.

For the D500, a bent monochromator on a Co tube ($\lambda = 0.1789$ nm) provides a relatively intense beam, but the divergence of the beam is significant and only two axes are computer controlled. The orientation of the crystal on the sample holder can only be done by hand and is limited to a rotation of the sample in its plane.

For the HRD, the Cu $K\alpha_1$ beam ($\lambda = 0.154059$ nm) is filtered by a Bartels 4-crystal monochromator which results [24] in a very small divergence (12 seconds of arc). The sample can be moved with 3 translational and 3 rotational degrees of freedom, allowing to select with precision the diffraction point in the reciprocal space.

The geometry of the DCI-D23 diffractometer at LURE is very similar to the HRD one, but the strong beam intensity and the ability to select the wavelength permit the use of contrast enhancing anomalous dispersion that is very useful in case of neighbouring elements such as Co and Mn.

The shape of the spectra peaks can be attributed to several origins. On the one hand, the mosaic distribution in the sample, which already exists in the buffer layer, results in a broadening of the peaks that appears as arcs at constant diffraction vector Q. On the other hand, the width of the peak is linked to the finite correlation length, due to the numerous defects generated during the growth, and the strain in the layers. The broadening is different in the growth direction (Q_Z direction) as compared to the growth plane (Q_X direction) since, due to the interfaces, the correlation length may be strongly limited in the growth direction.

The effect of stacking faults on the X-ray diffraction patterns has been analysed in detail [25]. In this study, the interest lies in the stacking faults generated during the growth. The diffuse intensity distribution varies strongly when α, the probability of a stacking fault appearing in the fcc phase, increases from 0 (pure fcc) to 1 (pure hcp). Consequently, scanning in the range between the $[113]_{\mathrm{fcc}}$ and $[10\bar{1}4]_{\mathrm{hcp}}$ peaks, as shown in Figure 1, the stacking fault density in the layers can be evaluated.

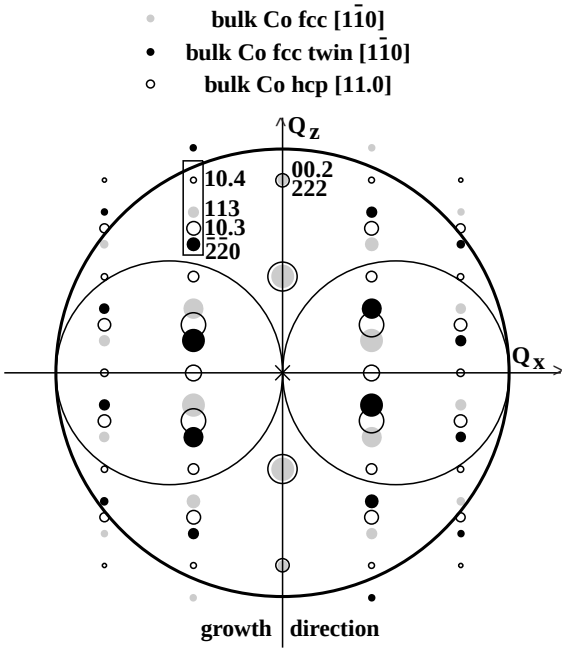

Fig. 1. Reciprocal lattice points corresponding to the possible, fcc, fcc-twin, and hcp, structure of Co. The growth direction is $[111]_{\rm fcc}$ ($[0001]_{\rm hcp}$). The outer circle represents the limit due to the wavelength ($\lambda = 0.1789$ nm). The inner circles represent the limits for reflection (outside of the circles) and transmission (inside) geometries. The rectangle in the upper left part of the figure corresponds to the section used for the diffracted intensity measurements (rocking curves in asymmetric geometry).

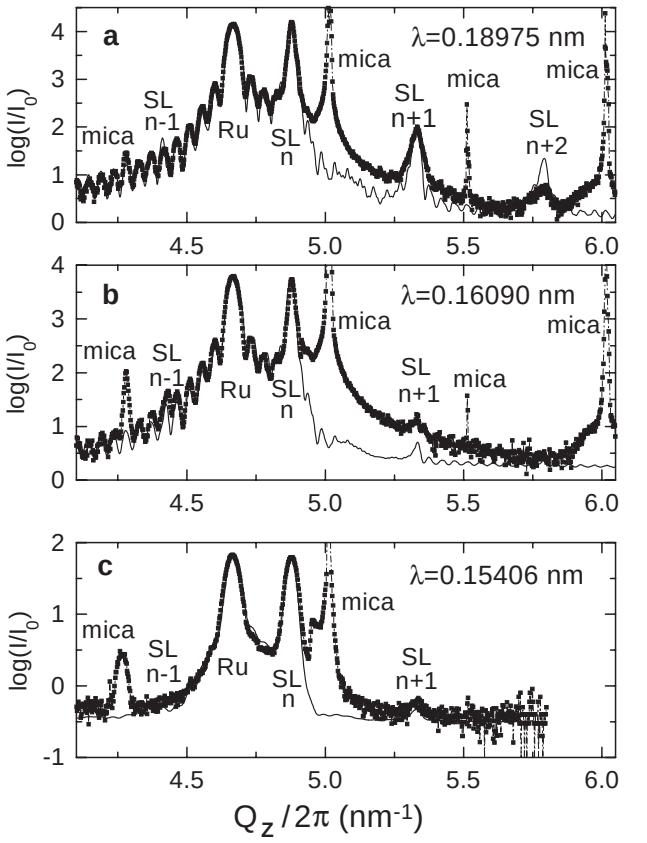

Fig. 2. $\theta/2\theta$ X-ray diffraction from the multilayer [Co 2 nm/Mn 0.6 nm] $\times$ 30 obtained at LURE (a, b) and at the laboratory (c). Comparison of the experimental data and the simulation as described in Section 2.3.

2.2 Experimental data and qualitative analysis

2.2.1 X-ray diffraction in symmetric geometry

The scanning using the HRD diffractometer, in order to examine the multilayer periodicity, was performed along the Q_Z axis of the reciprocal space. All the spectra obtained have a shape similar to that shown in Figure 2: the Ru peak is clearly visible at $Q_Z/2\pi = 4.67$ nm^{-1}, and the fifth order peak at $Q_Z/2\pi = 5.05$ nm^{-1} of the mica substrate is very intense. The impurity concentration in mica could explain the supplementary small peaks, when they appear, at $Q_Z/2\pi$ of 5.5, 4.5 and 4.25 nm^{-1}. The superlattice main peak (labelled SL_n), corresponding to the average lattice parameter along the growth direction, has an intensity comparable to that of the Ru peak. The superlattice period gives rise to weak satellites (labelled SL_{n+2}, SL_{n+1} and SL_{n-1}). The intensity of these satellites is related to the atomic contrast between Co and Mn which is small when scanned at $\lambda = 0.154059$ nm (Fig. 2c). Generally, only one or two satellites could be observed; their presence shows a limited interdiffusion and the good quality of the superlattice.

Contrast enhancing anomalous diffraction conditions were employed at LURE to study a sample [Co 2 nm/Mn 0.6 nm] $\times$ 30 (see Fig. 2a, b). The X-ray wavelengths were chosen to be 5 eV below the K edge of Mn ($\lambda = 0.18975$ nm) and of Co ($\lambda = 0.1608$ nm). The finite thickness fringes from the Ru buffer layer are well resolved in spectra a and b, while they are not visible in spectrum c. The better signal to noise ratio at LURE, as well as the better angular resolution, explain this difference. In spectra a, the superlattice reflections SL_{n+1} and SL_{n+2} are also clearly resolved.

From their position one can deduce the actual period of the superlattice, and consequently the actual thickness of the layers. As a matter of fact, the nominal thickness can differ notably from the actual one due to either a difference between the sticking ratios of the atoms on the quartz micro balance and on the sample, or to a difference between the density of the phases deposited on the quartz and on the sample (especially for Mn). Using the simple hypothesis that the ratio between the nominal and actual thickness is constant for each element, and plotting the ratio between the actual and the nominal period, we can calculate the correction factors for Co ($r_{\rm Co}$) and Mn ($r_{\rm Mn}$) in the specific growth conditions. The general trend for most of the samples is: $r_{\rm Co} \simeq 1$ and $r_{\rm Mn} \simeq 0.46$. Nevertheless, the samples with smaller quantities of Mn deviate from that trend. In these samples, where almost only cobalt is deposited, the correction factor for Co is close to 0.8,

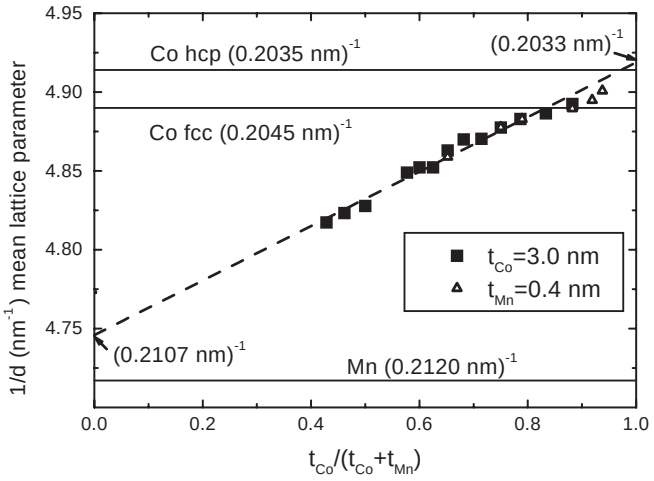

Fig. 3. Inverse of the mean lattice parameter in the growth direction for both Series I and II as a function of the relative nominal thickness of Co. ($\frac{1}{d} = \frac{(n_A+n_B)}{(n_A d_A+n_B d_B)} = \frac{t_A}{t_A+t_B}\frac{1}{d_A} + \frac{t_B}{t_A+t_B}\frac{1}{d_B}$.)

a value that has already been reported for Co/Ru multilayers [23]. Therefore, it seems that the sticking coefficient of Co is not constant in these layers, and the presence of Mn increases it from 0.8 to almost 1. This is not surprising as the presence of an ordered CoMn phase in the phase diagram [26] is an indication of a strong interaction between Co and Mn atoms.

Figure 3 shows the variation of the inverse of the average lattice parameter in the growth direction, as deduced from the superlattice main peak SL_n position for both Series I and II, as a function of the relative nominal thickness x_{Co} of Co. The variation is expected to be linear, with extrapolated values at $x_{Co} = 0$ and $x_{Co} = 1$ corresponding to the lattice parameters along the growth direction for the Mn and Co layers respectively. The result of the linear regression is shown in Figure 3; note that there are no errors presented, the experimental error bars for 1/d being smaller than the symbol size. Nevertheless, the use of the nominal thickness values introduces an additional error.

In this figure, the bulk values of the lattice parameter for the two possible Co phases are presented, as well as the expected lattice parameter for the γ-Mn phase when extrapolated to room temperature. As can be seen, the extrapolated and bulk values are in reasonable agreement. The extrapolated Co lattice parameter is smaller than the bulk fcc one, whereas the observations in asymmetric geometry have shown an expansion of the lattice parameter in the growth direction. The asymmetric geometry result is rather reliable, and this allows an estimation of the error on the extrapolated parameter. This error could be attributed to the uncertainty introduced by the use of nominal thickness values, as well as the existence of strain or structural changes within the layers.

In the samples having the thickest Co layers, the value of the lattice parameter along the growth direction is in between the fcc and the hcp lattice parameter, which is in agreement with the existence of a two phase mixture in these samples (for details, see discussion section).

The correlation length along the growth direction, as deduced from the SL_n peak width in Q_Z, does not vary in Series II samples, in contrary to what was observed in Series I. It remains equal to about one third of the multilayer thickness (∼25 nm). This large correlation length could be explained easily by the fact that the Mn layers are not continuous (this assumed sample correlation length is probably slightly under-estimated as the beam coherence length is about 100 nm). The coherence of the periodicity in the growth direction is not perturbed by a concentration of Mn that only expands the lattice locally.

The FWHM of the rocking curves from Series II samples is almost constant (about 1.4°), whereas the buffer layer rocking curve width is about 1.3°. This measurement does not allow a separation between the contribution of the mosaic distribution and the one due to the finite in-plane correlation length. Indeed, the width of the rocking curves is mainly related to the substrate on which the multilayers are grown.

2.2.2 X-ray diffraction in asymmetric geometry

Asymmetric rocking curves were obtained from the rectangular area shown in Figure 1. Figure 4 shows the evolution of the X-ray diffraction intensity (obtained with the D500) near the $[10\bar{1}3]_{hcp}$ and $[10\bar{1}4]_{hcp}$ Bragg peaks of Ru and Co, and near the $[113]_{fcc}$ and $[\bar{2}\bar{2}0]_{fcc\text{-}t}$ Bragg peaks of the normal and twin fcc Co, respectively. The position of these peaks, calculated from bulk parameters, is shown in the upper part of Figure 4. The Ru peak is always the most intense, as expected from its strong diffusion factor and the coherence of the buffer layer, although the total thickness of Ru (25 + 10 nm) is comparable to the total thickness of Co.

For each intensity map, the contribution of Ru and Co/Mn layers are found at $Q_X/2\pi$ of 4.3 and 4.6 nm^{-1}, respectively (see Fig. 4). For the Co/Mn layers, it incorporates the following peaks: $[\bar{2}\bar{2}0]_{fcc\text{-}t}$, $[10\bar{1}3]_{hcp}$, $[113]_{fcc}$, and $[10\bar{1}4]_{hcp}$. The additional peaks (at $Q_X/2\pi = 3.9$ nm^{-1} and $Q_Z/2\pi = 9.3$ or 8.7 nm^{-1}) can be attributed to mica.

The data corresponding to constant Q_X were extracted and fitted with Gaussian shape lines. The smooth background was taken into account as a linear contribution. Corrections for the total number of atoms and the variation of the scattering factor have also been taken into account. The procedure was validated using the intensity of the $[10\bar{1}3]$ and $[10\bar{1}4]$ Ru peaks. The expected factor of 3 in the intensities was indeed observed. The result is plotted as a function of Q_Z (Fig. 5) for the contribution of Co/Mn.

For all samples the fcc peaks are clearly resolved. For the samples with thinner Co layers, stacking faults are present, giving rise to a diffuse line which broadens the $[113]_{fcc}$ and $[\bar{2}\bar{2}0]_{fcc\text{-}t}$ peaks towards the $[10\bar{1}3]_{hcp}$ position. This stacking fault contribution increases in the samples with thicker Co layers, gradually giving rise to a weak peak

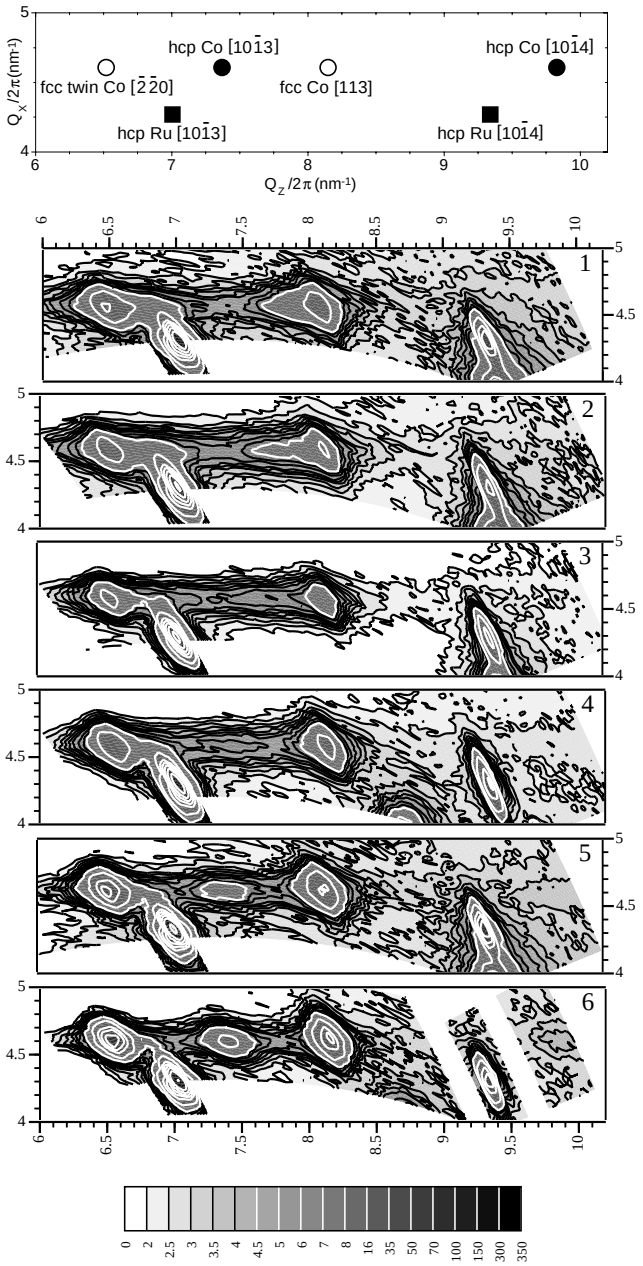

Fig. 4. Iso-intensity maps of the X-ray diffraction from the rectangle section in Figure 1 and for different multilayers having always 0.4 nm of Mn. Top, positions of the Bragg peaks in the measurement rectangle, (1) to (6) maps from samples 1 to 6.

at the [10$\bar{1}$3] position. The hcp [10$\bar{1}$4] peak appears only for samples 5 and 6 (t_{Co} of 4.5 and 6 nm, respectively), but even in these samples, the Co layers are mainly fcc. Detailed analysis, using a Monte-Carlo like simulation of the stacking fault density, is given in Section 2.3.

The residual strain in the Co layers was evaluated using the position of the peaks. For this purpose, the correctness of the experimental setup was verified using the Ru Bragg peaks, since they appear at the expected positions.

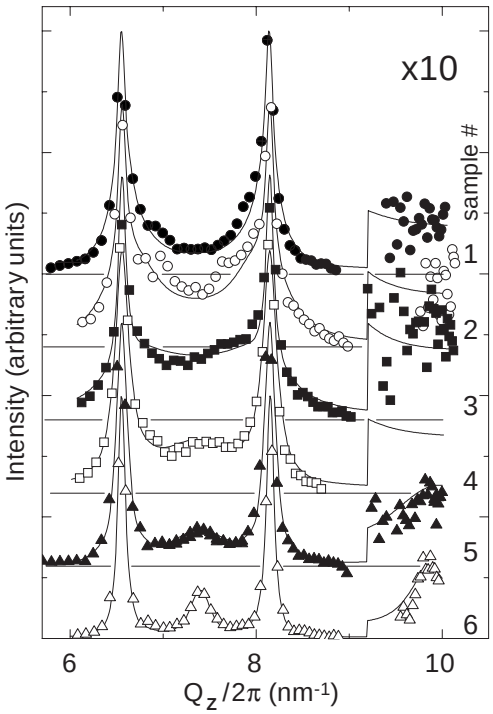

Fig. 5. Intensity profile along the $[10\bar{1}l]_{\mathrm{hcp}}$ line measured for samples 1 to 6 extracted from the maps shown in Figure 4. The solid line corresponds to the best simulation using the model presented in Section 2.3.

In the growth direction (Q_Z), the resolution is good, and the evolution of the Cobalt parameter from a 1% strained value, for sample 1 ($t_{\mathrm{Co}} = 0.75$ nm), to the fcc bulk one, for sample 6 ($t_{\mathrm{Co}} = 6$ nm), is clear. The resolution along the Q_X direction is not as good. For sample 1 (cobalt thickness ∼3.5 monolayers), the cobalt in-plane strain is $\Delta a/a = 1.5 \pm 1.0\%$. This is not surprising as most of the Co atoms are in the vicinity of Mn atoms whose atomic volume is larger than that of Co. The in-plane parameter decreases with increasing thickness of the Co layer, and eventually reaches its bulk value within the error margin in sample 6. As a matter of fact, it would be surprising if 0.4 nm of Mn could strain 6 nm of Co. Any different evolution of the two lattice parameters would correspond to a trigonal deformation, but the Q_X resolution does not permit a quantitative estimation of the presence of such deformation. In conclusion, the lattice expansion in the Co layers can be attributed to the Mn, and this strain is relaxed gradually as the thickness of the Co layer increases.

2.3 Quantitative analysis of the results

2.3.1 X-ray diffraction in symmetric geometry

Quantitative results were obtained from the interpretation of the experimental data with the aid of a computer simulation using the kinematic approximation. The in-house

developed software that was used has been already described elsewhere [20,27]. The needed refinement was not straightforward due to the large number of parameters involved and due to the fact that the structure of the Mn layers is not known, and, of course, the main obstacle is the mica substrate intensity. The substrate signal is not reproducible as it varies from sample to sample because natural mica was used, and the existing variety of impurities does not allow an accurate prediction of the signal.

The parameters for the simulation are the number of atomic planes for each layer (n_{Co} and n_{Mn}), the interplanar distances along the growth direction in each layer (c_{Co} and c_{Mn}), and the density in the growth plane (s_{Co} and s_{Mn}, which are related to the in plane lattice parameters a_{Co} and a_{Mn}). The fluctuation of the layer thickness was taken into account as a Gaussian distribution with FWHM σ (averaging the intensity over a large number of 'samples') [27]. Additionally, a linear concentration profile was used to describe the interface gradient. The slope p_1 (p_2) gives the Co (respectively Mn) concentration variation on a monolayer at the Co/Mn (respectively Mn/Co) interface.

The lattice parameter of the cobalt has been found to be similar to that of the bulk fcc cobalt, in agreement with the NMR and asymmetric geometry X-ray diffraction results. The Mn plane spacing in the growth direction was found to be 0.209 nm, a value similar to the one derived with data extrapolation from Figure 3 (0.2107 nm). The solid lines in Figure 2 represent the best fitting simulation obtained using the following parameters: $n_{\mathrm{Co}} = 9.4$ and $n_{\mathrm{Mn}} = 1.3$, $c_{\mathrm{Co}} = 0.2045$ nm and $c_{\mathrm{Mn}} = 0.209$ nm, $s_{\mathrm{Co}} = 9.24$ at/nm^2 and $s_{\mathrm{Mn}} = 6.86$ at/nm^2. These yield a thickness of $t_{\mathrm{Co}} = 1.92$ nm and $t_{\mathrm{Mn}} = 0.28$ nm, and assuming a dense six-fold symmetry, as in the fcc (111) plane, in-plane atomic distances of $a_{\mathrm{Co}} = 0.25$ nm and $a_{\mathrm{Mn}} = 0.29$ nm. The experimentally found width of the main peak, which is related to the correlation length along the growth direction, can be reproduced satisfactory by a coherent diffraction of 19 bilayers.

It was found that there is no significant interdiffusion ($p_1 = p_2 = 1$) and a small dispersion of the layer thickness $\sigma = 5\%$. The accuracy of the values for these interface parameters is limited by the presence of the mica peak tail. As far as interdiffusion is concerned, RHEED and NMR observations suggest island growth of Mn, allowing the coherence of the Co layers to be retained through a discontinuous Mn layer, especially since the Mn layer thickness is less than 2 monolayers.

The errors on the different parameters are estimated from the different sensitivity of the simulation to the value of each of them. These errors were 0.5% for c_{Mn} and 5% for a_{Mn} (10% for s_{Mn}). The large error value for a_{Mn} (s_{Mn}) is due to inconsistencies in the fitting of the SL_{n-1} peak at the concerned wavelengths. In fact, the large difference between the surface density of Co and Mn, a ratio of 0.75, suggests some disorder in the Mn layers due to the existence of a large number of vacancies. The value of a_{Mn} is thus an average and cannot yield precise information on the Mn structure. Nevertheless, the Mn layers in these samples are so thin that it is not appropriate to talk about 3D structure. The results from anomalous diffraction are in agreement with information obtained from *in situ* RHEED [21] showing an incoherent growth of Mn on Co with an average in-plane parameter of 0.29 nm for the first deposited monolayer.

The values obtained from the anomalous diffraction simulation were verified in simulation of other spectra for data recorded at the laboratory. The only adjustable parameters here were the thickness of Co and Mn layers, and the good agreement found in the results confirmed the validity of the method.

Low in-plane density exists for the thicker Mn layers, $a_{\mathrm{Mn}} \sim 0.29$ nm assuming a close packed stacking. The Mn lattice parameter is larger than the Co both in-plane (16%) and in the growth direction (2.2%). Thus the Mn structure would be trigonal ($c/a = 0.72$ instead of 0.816 for fcc Mn) and, if there is one atom per unit cell, the size of the manganese atom would be large. Such large manganese atomic volume has been already reported [28,29] for other systems. Data obtained from the structure inside the Mn layers did not illuminate the situation [20], thus there is no direct information on the structure of the Mn layers.

2.3.2 X-ray diffraction in asymmetric geometry

Monte-Carlo simulations were performed for a large number of 'samples' and the corresponding X-ray and NMR spectra were calculated. Experimentally, the X-ray diffraction intensity has been measured around the area defined by the $[10\bar{1}4]_{\mathrm{hcp}}$, $[113]_{\mathrm{fcc}}$, $[10\bar{1}3]_{\mathrm{hcp}}$ and $[\bar{2}\bar{2}0]_{\mathrm{fcc\text{-}t}}$ peaks; the simulation was performed using the lines parallel to the Q_Z axis corresponding to the above mentioned peaks, as well as to the $[0002]_{\mathrm{hcp}}$ and $[111]_{\mathrm{fcc}}$ peaks (symmetric geometry).

The 'samples' are considered as disks with a diameter of 20 unit cell parameters, thus containing around 150 atoms. This size has been found to be large enough so that the results become size independent. The atoms in the planes have an hexagonal arrangement and can occupy 3 sets of positions, corresponding to the A, B and C positions of an fcc structure. We will use this notation to describe the type of the plane (A, B or C). The type of the first plane is chosen randomly as well as the initial stacking: normal fcc (ABC stacking) or twin fcc (ACB stacking). The 'sample' was constructed plane by plane, at each step the presence (or the absence) of a stacking fault was determined by comparing a randomly generated number with the probability α. For the thickness of the disk, the correlation length of the superlattice was used, thus the equivalent of the experimentally measured intensity was obtained as the sum of the calculated intensities for a large number of disks (typically 3000). The main parameters of the simulation are the probability of appearance of a stacking fault (α) and the correlation length corresponding to the number of planes for each sample (N_{plan}).

We assumed that the parameter α, the occurrence probability of a stacking fault within a grain, could

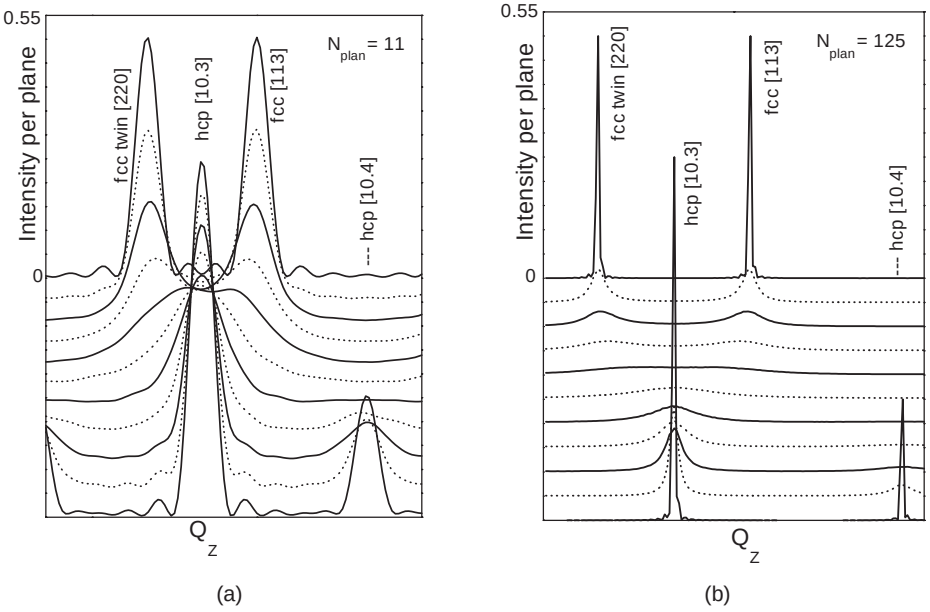

Fig. 6. Simulated intensity along the $[10\bar{1}l]_{\rm hcp}$ line for different α and $N_{\rm plan}$. (a) $N_{\rm plan} = 11$, (b) $N_{\rm plan} = 125$.

completely describe the state of a grain (as suggested, among others, by Guinier [25]). This way, we do not take into account any interaction between stacking faults.

The growth plane of the samples is the six-fold symmetry plane common to both fcc ((111) plane) and hcp ((0001) plane) structures, and each time, at the beginning of a new plane, the first atom could be deposited aligned either with the atoms of the penultimate plane or not. The first option is always followed in the case of hcp growth, while the second is valid in the case of fcc growth. As the energy difference between both stacking sequences is very small in cobalt, the cobalt growth very often takes place with a lot of stacking faults along the growth direction.

The intensity of the $[111]_{\rm fcc}$ Co peak, along Q_Z, is independent of α. The peak height is proportional to $N_{\rm plan}^2$ and the FWHM of the peak is proportional to $1/N_{\rm plan}$. This is expected, as long as there is no change in the plane spacing according to the local stacking. Experimentally, the variation of the perpendicular-to-plane parameter between an fcc (0.2045 nm) and an hcp (0.2035 nm) stacking is 0.5%, and that can be considered as negligible as long as $N_{\rm plan} \leq 200$, which is always true in our case.

Along the line parallel to Q_Z, corresponding to the line through the peaks $[\bar{2}\bar{2}0]_{\rm fcc\text{-}t}$ and $[10\bar{1}4]_{\rm hcp}$, the height and width of the peaks depend strongly on α as well as on $N_{\rm plan}$. Figure 6 shows the dependency of the intensity divided by $N_{\rm plan}^2$ on α along this line for $N_{\rm plan} = 11$ and 125. In a perfect structure, these intensities would have a value of 0.5 for both $[113]_{\rm fcc}$ and $[\bar{2}\bar{2}0]_{\rm fcc\text{-}t}$, and 0.75 and 0.25 for the $[10\bar{1}3]_{\rm hcp}$ and $[10\bar{1}4]_{\rm hcp}$ respectively. The width of the peaks corresponds in this case to the normal diffraction showing the classical $[\sin(qN_{\rm plan}a)/(qN_{\rm plan}a)]^2$ variation.

With α increasing from 0 to 1, the intensity of the fcc peaks decreases, and a background intensity appears between them. For values of α between 0.3 and 0.6, a large intensity is observed centred on the $[10\bar{1}3]_{\rm hcp}$ peak and extending between the two fcc peaks. As α increases, this intensity distribution takes the form of the $[10\bar{1}3]_{\rm hcp}$ peak, while only for values of α larger than 0.7 a peak is clearly observed at the $[10\bar{1}4]_{\rm hcp}$ position. The variation of H_4/H_3, the ratio of the maxima of the hcp peaks, is plotted as a function of $N_{\rm plan}$ in Figure 7. It saturates very rapidly for thick samples when a significant number of stacking faults is present in the hcp structure ($\alpha \leq 0.8$). The same behaviour is observed for L_3, the width of the $[10\bar{1}3]_{\rm hcp}$ peak. This implies that, for samples with intermediate values of α, the shape of the spectra is independent of the number of atomic planes. In the case of high stacking fault densities, concerning both fcc and hcp

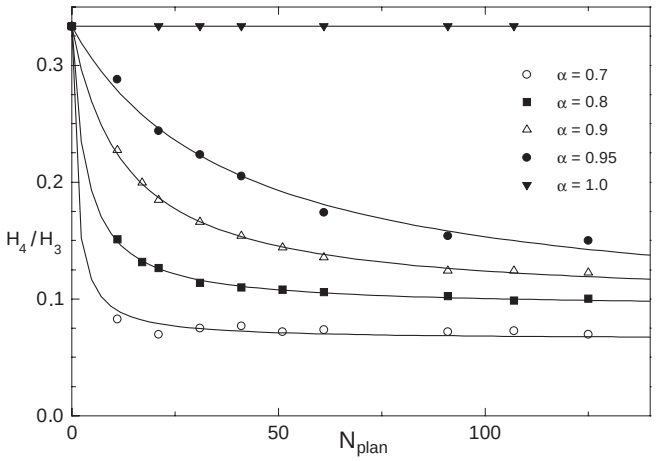

Fig. 7. H_4/H_3 dependence on $N_{\rm plan}$, where H_4/H_3 is the ratio between the $[10\bar{1}4]_{\rm hcp}$ and $[10\bar{1}3]_{\rm hcp}$ peaks.

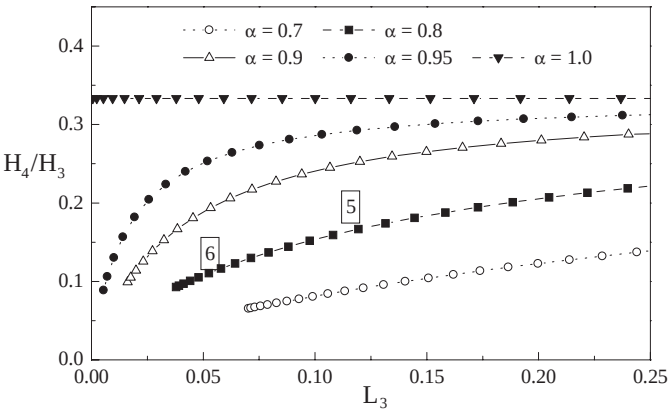

Fig. 8. H_4/H_3 as a function of L_3 for different values of α and $N_{\rm plan}$. The points corresponding to samples 5 and 6 are shown as rectangular areas, representing the errors for both values.

structures, it means that the structural correlation length is smaller than the sample thickness.

The X-ray experimental spectra (Fig. 5) clearly incorporate two contributions. Thus, we assume that the samples are formed of two types of grains: fcc-like and hcp-like grains with different correlation lengths and stacking fault densities. Comparing the experimental spectra with the one obtained from a perfect fcc having a number of planes that corresponds to the Co layer thickness, we see that the experimental fcc peaks are much narrower, therefore the correlation length in the samples ranges over several Co layers. The correlation length along the Q_Z direction has been found to be very similar in all the samples for the $[111]_{\rm fcc}$ ($[0002]_{\rm hcp}$) peak, with a value around 25 nm. This value was used as the correlation length for the fcc stacking simulation, and this corresponds to $N_{\rm plan} = 125$.

The spectra simulation was executed in two steps, first the value of α in the fcc phase was deduced from the width of the fcc peak using $N_{\rm plan} = 125$. Then the intensity of this contribution was subtracted from the spectra to get the approximate value of the hcp contribution. The characteristic plot of that hcp contribution, H_4/H_3 *versus* the width L_3 is shown in Figure 8 where the points representing these quantities have been calculated for different values of α and for varying values of $N_{\rm plan}$. The best choice of values for α and $N_{\rm plan}$ has been found for samples 5 ($N_{\rm plan} = 8$) and 6 ($N_{\rm plan} = 27$) when α is close to 0.8. For the other samples, where α is intermediate ($0.3 < \alpha < 0.6$), the intensity per plane is independent of $N_{\rm plan}$, and a value of $N_{\rm plan} = 125$ was used for the calculations. Finally, the experimental spectra was fitted to these two contributions to get the proportion of the two phases. The results are given in Table 1.

3 Nuclear Magnetic Resonance

3.1 Experimental details

Nuclear Magnetic Resonance (NMR) in ferromagnetic samples is very sensitive to the crystallographic and magnetic surroundings of the resonant nucleus. The nucleus hyperfine field is modified by changes in the occupancy or in the position of its near neighbour sites: NMR is sensitive to both topological and chemical environment. Hence, it is possible to differentiate a cobalt nucleus in an fcc Co environment from one in an hcp Co surrounding as their resonance frequencies are quite different: 217 MHz for fcc Co and 226 MHz for hcp Co (when the local moment is perpendicular to the c-axis, as it is in the case of the studied superlattices). These frequency values may be slightly modified due to the existence of elastic strains [30]. NMR experiments performed under high pressure show that the change in resonance frequency f due to a change in the atomic volume V is given by $\delta f/f \approx -\delta V/V$ [31]. In addition, intermediate peaks between the fcc and hcp ones, originating from atoms at stacking faults, can be observed [32].

In a perfect crystal the peaks are narrow (FWHM $<$ 1 MHz), but a broadening can appear due to alloying or to crystallographic defects. In multilayers both effects coexist: alloying at the interfaces and crystallographic defects inside the layers as well as at the interfaces. Qualitatively, the Co NMR spectra in multilayers consist of a main line corresponding to the bulk of the Co layers (Co surrounded by Co only) and of a tail arising from interfacial Co atoms that have at least one alien atom in their nearest neighbour shell [33]. The shape of the main line yields information about the crystallographic structure of the layers, whereas the shape of the tail gives an insight on the nanostructure, roughness and admixture of the interfaces.

Zero field Co NMR spectra have been obtained at 1.5 K using an automated frequency scanning broadband spectrometer with phase coherent detection. The spectra were corrected for the frequency dependent enhancement factor and the ω^2 dependence of the NMR signal [34].

3.2 Experimental data

Both series of Co/Mn samples were studied using NMR. The experimental results obtained from Series I are presented here as a reminder of the structural changes, on an atomic scale, that occur when the thickness of the Mn layer increases. This evolution, at constant Co thickness (3 nm) and varying Mn thickness ($t_{\rm Mn}$), is displayed in Figure 9. For the sample having the thinnest Mn layers (0.4 nm), the Co layers are strained and have an fcc structure, as it becomes evident from the sharp main peak at 215 MHz, instead of the 217 MHz peak for bulk fcc Co. However, the shoulder peak close to the main peak and at higher frequencies, indicates the existence of a considerable number of stacking faults in the fcc structure. In samples having thicker Mn layers, observations show that

Table 1. The different phases deduced from X-ray and NMR spectra analysis, the corresponding α (stacking fault probability) and their occurrence percentages. For each sample the number, the nominal thickness in nm, the actual thickness in monolayers and the number of bilayers N are given.

Sample				X-rays						NMR					
#	t_{Co}		N	small α		medium α		large α		small α		medium α		large α	
	nm	ML		α	%	α	%	α	%	α	%	α	%	α	%
1	0.75	3	65	0.05	33	0.30	67								
2	1.2	5	47	0.05	22	0.30	78					0.45	100		
3	1.5	6	40	0.05	26	0.30	14	0.40	60	0.09	29	0.42	71		
4	3.0	12	22	0.10	65			0.50	35	0.16	65			0.66	35
5	4.5	18	15	0.08	79			0.84	21	0.08	62			0.63	38
6	6.0	24	12	0.05	77			0.84	23	0.06	66			0.66	34

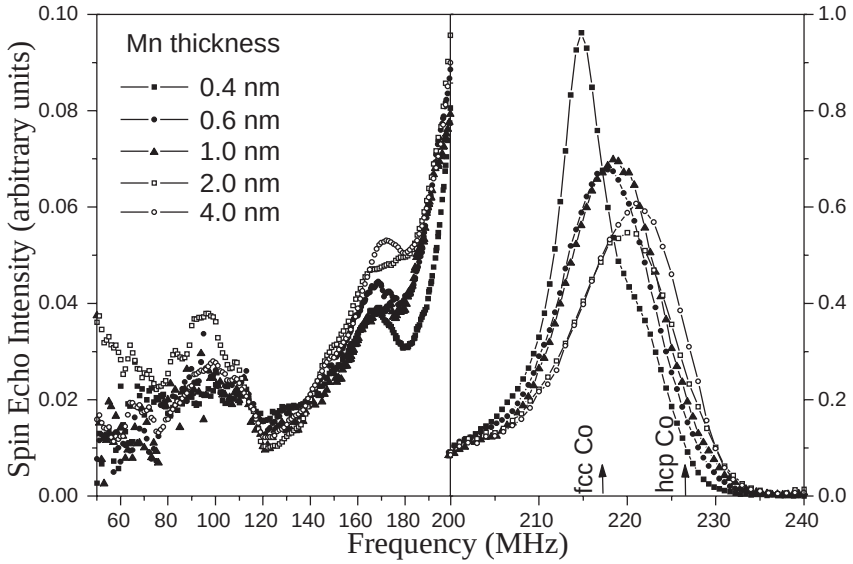

Fig. 9. Evolution of the ^{59}Co NMR spectra in the Series I samples (constant Co thickness 3 nm) as a function of the Mn layer thickness. Left, interface spectrum (Co surrounded by at least one Mn atom). Right, bulk Co layers spectrum (Co embedded in Co).

the main peak shifts towards higher frequencies, *i.e.* towards the hcp position, and broadens. Note that NMR results, which reflect the average short range structure, do not show an abrupt transition around $t_{Mn} = 1.6$ nm but a rather continuous evolution between $t_{Mn} = 0.4$ nm and $t_{Mn} = 2$ nm. For $t_{Mn} > 2$ nm the shape of the spectra does not evolve anymore. In fact, at large Mn layer thickness, the Co layer never achieves the perfect hcp stacking.

Experimentally, the main peak appears at 222 MHz, compared to 226 MHz for bulk hcp Co. If this diminution of the resonance frequency was to be attributed to residual strain, it would correspond to an atomic volume change of $\delta V/V$ of about 2%. However, the width of the peak, which covers the full frequency range from fcc to hcp Co, indicates that the maximum at 222 MHz can be better interpreted by the coexistence of hcp and fcc stacking.

The subsidiary peaks at lower frequencies are generated by the interfacial Co atoms. The spectra show that the interface nanostructure does not evolve greatly with increasing Mn thickness, except for a small increase in intensity and a shift towards higher frequencies comparable to that of the main peak. From the relative intensity between the interfacial contribution and the total Co spectra, the amount of Co atoms in contact with Mn is estimated to an equivalent Co thickness of about 0.3 nm (1.5 monolayers) at each interface (for a more detailed analysis see Sect. 3.3).

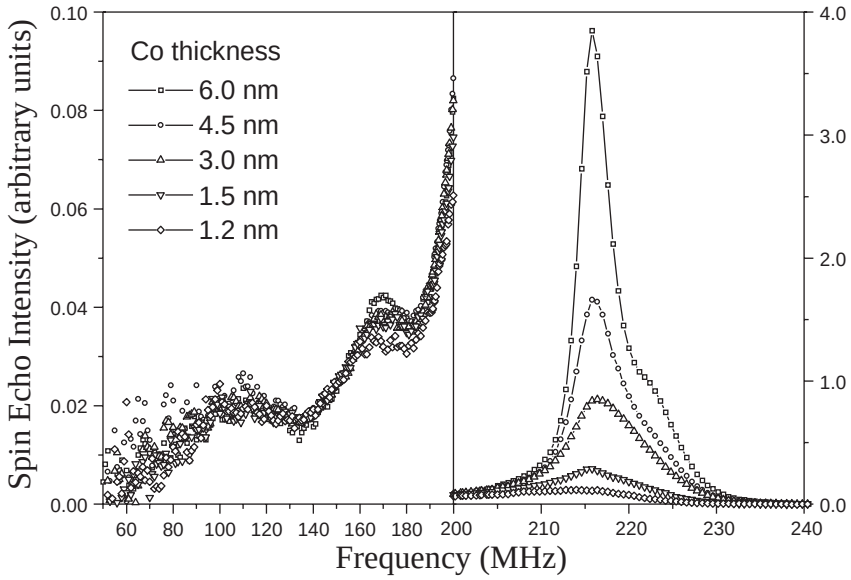

Fig. 10. Evolution of the ^{59}Co NMR spectra in the Series II samples (constant Mn thickness 0.4 nm) as a function of the Co layer thickness. The spectra lines are normalised to t_{Co} so that the intensities of the peaks are comparable. Left, interface spectrum (Co surrounded by at least one Mn atom). Right, bulk Co layers spectrum (Co embedded in Co).

The NMR spectra of the Series II with constant Mn layer thickness of 0.4 nm are shown in Figure 10. For the largest Co layer thickness (6 nm), the peak position (216.5 MHz) of the main resonance line corresponds to bulk, slightly expanded, fcc Co. The shoulder on the high frequency side of this line is due to hcp stacking faults. When the Co thickness decreases, the main peak broadens and shifts towards lower frequencies because of the increased expansive strain due to the larger lattice parameter of Mn compared to Co. For the smallest Co layer thickness, 0.75 nm (0.6 nm actual), only a weak NMR signal (not shown) could be observed; this is consistent with the above mentioned fact that at each interface about 0.3 nm of Co are involved and, therefore, the Co layers are weakly ferromagnetic for this sample because the interfacial mixing extends over the whole of the layer. The detailed changes to the shape of the main line are analysed in Section 3.3.

The low frequency parts of the spectra are almost identical, which shows that the nanostructure and the composition at the interfaces do not change with increasing Co thickness. Between the bulk peak and the interface contribution, there is a fraction of Co nuclei, that resonates in the frequency range 200–210 MHz, which does not clearly belong either to the bulk or to the interface. Usually the signal in this range arises from grain boundaries and increases linearly with layer thickness [35]. Here, a small increase of this signal is indeed observed at small thickness but it reaches an upper limit at larger thickness. Therefore this signal definitely corresponds to Co atoms close to the interface. Two explanations are possible for this: (i) crystallographic, due to the presence of dislocations in the vicinity of the Mn layer, or (ii) magnetic, due to an extended influence of Mn, further than the first neighbours, on the hyperfine field and the magnetic moment of Co.

3.3 Analysis of the results

3.3.1 Interface structure

In order to obtain information on the composition at the interfaces, we created a model for the interface spectra. As discussed elsewhere [34,36], the basis for interface spectra modeling is the shift of the Co NMR frequency resulting from the presence of alien elements in the nearest neighbour shell of a Co nucleus: this shift gives rise to successive satellites to the main peak which correspond to nearest neighbour configurations with 1, 2, etc. alien neighbours and the intensity of which scales with the fraction of volume occupied by the corresponding configuration. For Mn, our measurements in bulk CoMn alloys show that the satellite spacing is ∼45 MHz per Mn neighbour. Considering a small admixture at the interfaces, a rather flat (111) interface would be expected and the spectra should show, at about 80 MHz, a dominant satellite peak corresponding to Co atoms having 3 Mn neighbours. Nevertheless, this is not the case: the dominant satellite is about 45 MHz only below the main peak, corresponding to Co atoms with 1 Mn neighbour, while a broad hump, in the 90–120 MHz region, arises from Co atoms having 2 or 3 Mn neighbours. Considering that only one monolayer of Mn has actually been deposited in Series II ($r_{\mathrm{Mn}} = 0.46$), a quick interpretation shows that, if this Mn layer was split into two atomic planes containing 50% Mn each, the spectrum obtained from the interface would be dominated by Co atoms with 1, 2 and, to a lesser extent, 3 Mn neighbours, in full agreement with the observations. A model

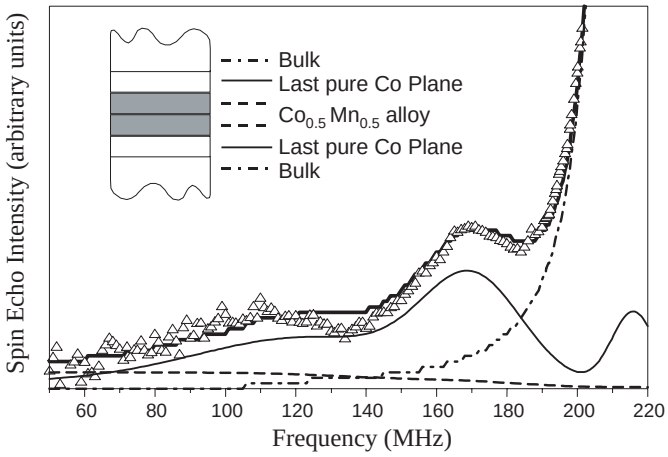

Fig. 11. Simulation (bold line) of the Co/Mn interfacial spectrum assuming that Mn atoms are randomly distributed in two atomic planes of a $Co_{0.5}Mn_{0.5}$ alloy. The contributions of the different components in the spectrum are shown as: dash-dots, the bulk of the Co layers, thin line, the last pure Co plane at the interface, and dashed line, the CoMn interface alloy.

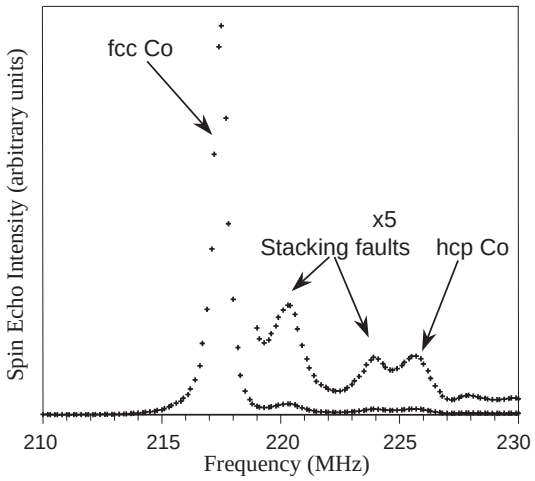

Fig. 12. Example of ^{59}Co spectrum as observed for a well crystallised bulk fcc Co sample. On the high frequency side of the main fcc peak, three contributions (shown magnified) related to stacking faults are visible. The highest frequency one corresponds to a hcp-like stacking (locally), which can be explained by the presence of 3 or more adjacent stacking faults.

[36] for the concentration profile at the interface confirms the fact that Mn is distributed over 2 atomic planes with a Mn content of 0.5 (Fig. 11). Consequently, there is no pure Mn plane in the Series II samples. When the Mn thickness increases, as in Series I, complete Mn planes are formed almost immediately between the two alloyed planes with only a small increase of Co-Mn admixture. This analysis is in agreement with the RHEED data [21] obtained during the Mn growth, which show 3D diffraction spots visible on the streaks, demonstrating that the deposition of the Mn layers does not follow a layer by layer growth mode. Nevertheless, the analysis of the NMR data shows that the interface roughness remains limited to one mixed plane in agreement with the XRD analysis.

3.3.2 Stacking faults in the Co layers

To obtain quantitative information concerning the hcp and fcc phases within the Co layers, as well as the crystalline quality, we analysed the shape of the bulk part of the NMR spectra using the same model as for the asymmetric X-ray diffraction data: the Co layers are considered as consisting of grains that differ in the fraction α of stacking faults they contain. As the NMR of a nucleus depends mostly on the nature and distance of the atoms in its nearest neighbour shell, the resonance frequency of a nucleus in a dense plane, say B, depends on the stacking, such as ABC (fcc like) or ABA (hcp like) and also on the stacking of its two adjacent planes. Hence the NMR signal depends on sequences of 5 planes, which may differ in the number and the position of stacking faults they contain. Starting from an arbitrary AB stacking, we have 2 possibilities for each of the subsequent planes, leading to 8 possible sequences; among these, only 6 sequences are different: $S_0 = \mathrm{AB}C\mathrm{AB}$, $S_{11} = \mathrm{AB}/A\mathrm{CB}$ and $S_{12} = \mathrm{AB}C/\mathrm{BA}$, $S_{21} = \mathrm{AB}/A/\mathrm{BC}$ and $S_{22} = \mathrm{AB}/A\mathrm{C}/\mathrm{A}$, $S_3 = \mathrm{AB}/A/\mathrm{B}/\mathrm{A}$, where "/" represents a stacking fault in the fcc sequence. The two other sequences, ABCA/C and ABC/B/C, are identical when read from right to left to $S_{11} = \mathrm{CA}/C\mathrm{BA}$ and $S_{21} = \mathrm{CB}/C/\mathrm{BA}$, respectively.

One expects the nuclei in the central plane of each of the 6 different sequences to resonate at different frequencies. Actually, the NMR spectra of the Co samples show only 4 resolved peaks, almost equally spaced: the fcc, the hcp, and two peaks in between (see Fig. 12 for an fcc sample and reference [32] for various fcc/hcp mixtures). In fact, one can see that the sequences S_{11} and S_{12} differ only by the position of the single fault which is found either before or after the central plane; then, one can easily imagine that the hyperfine field at this central plane does not really differ between these two configurations. As far as S_{21} and S_{22} is concerned, the same argument holds, the only difference being that the stacking faults are introduced in an initial hcp sequence. Indeed, they can be seen as $S_{21} = \mathrm{AB}A\mathrm{B}\backslash\mathrm{C} = \mathrm{CB}\backslash A\mathrm{BA}$ (when read from right to left), and $S_{22} = \mathrm{AB}A\backslash\mathrm{CA}$, where "\" represents a stacking fault in the hcp sequence. Therefore the model, as a result of these experimental observations, takes into account 4 peaks corresponding to configurations around a central plane having between 0 and 3 stacking faults. That means S_0 at ∼217.5 MHz (locally fcc), S_1 (S_{11} and S_{12}) at ∼220.5 MHz (1 fault, fcc dominant), S_2 (S_{21} or S_{22}) at ∼224 MHz (2 faults, hcp dominant) and S_3 at ∼226 MHz (locally hcp).

Assuming that stacking faults are not interacting, the intensity of the 4 peaks is constrained to scale with the binomial probability to find 0 to 3 stacking faults among 3 places in a sequence of 5 planes, which depends only on the concentration of stacking faults α. In the fitting

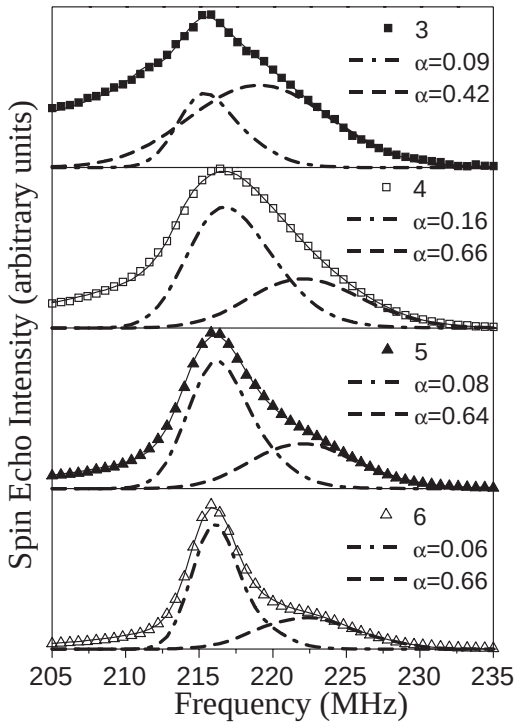

Fig. 13. Simulation of the NMR spectra from the bulk Co part in the Series II (samples 3 to 6) using two populations with different concentrations α of stacking faults ($\alpha = 0$ corresponds to perfect fcc and $\alpha = 1$ to perfect hcp).

procedure the relative positions of the 4 peaks were kept constant (within 0.5 MHz) but a shift of the whole spectrum was necessary in order to take into account the effect of strains. As shown in Figure 13, the bulk part of all the experimental spectra could be satisfactory simulated with two populations of 'grains', one dominantly fcc ($\alpha < 0.5$) and one dominantly hcp ($\alpha > 0.5$). For comparison with the results of the X-ray diffraction study, the quantitative results obtained are given in Table 1. They confirm that the fcc phase is dominant and of much better crystalline quality than the hcp phase.

3.3.3 Strains

Due to the structural changes which follow the increase of the Co layer thickness, it is difficult to observe the exact shift in frequency due to strains. From the fitting performed, the main fcc peak is found at 212 MHz for the thinnest Co layer, which represents a shift of ∼5 MHz from the resonance for bulk fcc Co. This 2% decrease in the resonance frequency corresponds to a relative volume change of +2%, that is 0.7% expansive strain, assuming that the expansion is isotropic. For larger Co thickness, the resonance frequency increases further to 216.5 MHz for $t_{\mathrm{Co}} = 6$ nm, a shift that corresponds to a residual strain of less than 0.2%.

4 Transmission Electron Microscopy

The transmission electron microscopy studies have been performed using a 200 kV Topcon 002B high resolution microscope (point to point resolution 0.18 nm) in Strasbourg and a JEOL 4000EX in Antwerpen.

Cross section TEM samples were prepared using a special procedure. First, the crystal orientation of the Ru buffer was obtained using X-ray diffraction in the asymmetric geometry and thus the samples could be cut into 2.5 mm × 10 mm pieces along the $[10\bar{1}0]$ and $[11\bar{2}0]$ directions, respectively. Two of these pieces were glued face to face with conducting epoxy, then sandwiched between two arcap (Cu-Ni alloy) half cylinders and inserted into an arcap tube with an outer diameter of 3 mm. This tube was cut into discs having a thickness of 0.4 mm. The discs were mechanically polished down to a thickness of ∼0.04 mm and ion thinned in a liquid nitrogen cooled dual gun, low angle ion mill. The ion current and the accelerating voltage during the thinning were optimised in order to minimise heating and ion-bombardment damage. Initially, the accelerating voltage was 5 kV and the ion current 2 mA, with a 4° angle of incidence. In the final stage, 2 kV and 1.5 mA were employed.

Figure 14 is a micrograph of the sample [Co 6 nm/Mn 0.4 nm]×12 with the electron beam direction along the $[11\bar{2}0]$ azimuth of both the Ru buffer layer and the hcp Co phase, which coincides with the $[1\bar{1}0]$ azimuth of the fcc Co. The damage visible at the top part of the imaged area is due to the ion thinning (amorphous and misoriented areas). The left side of the image is relatively thick and does not allow high resolution microscopy. The analysis was performed using the central part of the image where the flatness and continuity of the dense growth planes show that the irradiation damage is negligible, while the thickness is suitable.

The selected area diffraction pattern corresponding to the image is shown in the insert. The vertical direction being the growth direction, the inner lines on both sides of the central one are due to hcp Ru and the outer lines due to Co (superposition of fcc and hcp contributions with streaks due to stacking faults). The twins of the fcc phase appear with the same intensity, as expected, while the hcp contribution is smaller. In agreement with the X-ray diffraction results, the cobalt appears relaxed as its in-plane lattice parameter corresponds to the bulk fcc. No additional diffraction spots that could be attributed to Mn are visible. The Mn layers (∼0.92 monolayers) are too thin to be imaged directly.

In the image, strong contrast appears in regular intervals along the growth direction. The thickness of the manganese layers, as already mentioned, is too small to be directly imaged. Nevertheless, the distance between these lines of contrast and the position of the Ru buffer layer show that they appear exactly at the expected position of the thin Mn layers (indicated by long horizontal arrows). Their flatness over long distances, and the similarity with the images obtained from samples presenting a mixture of fcc and hcp phase due to an incomplete martensitic transformation, suggest that they originate from stacking faults

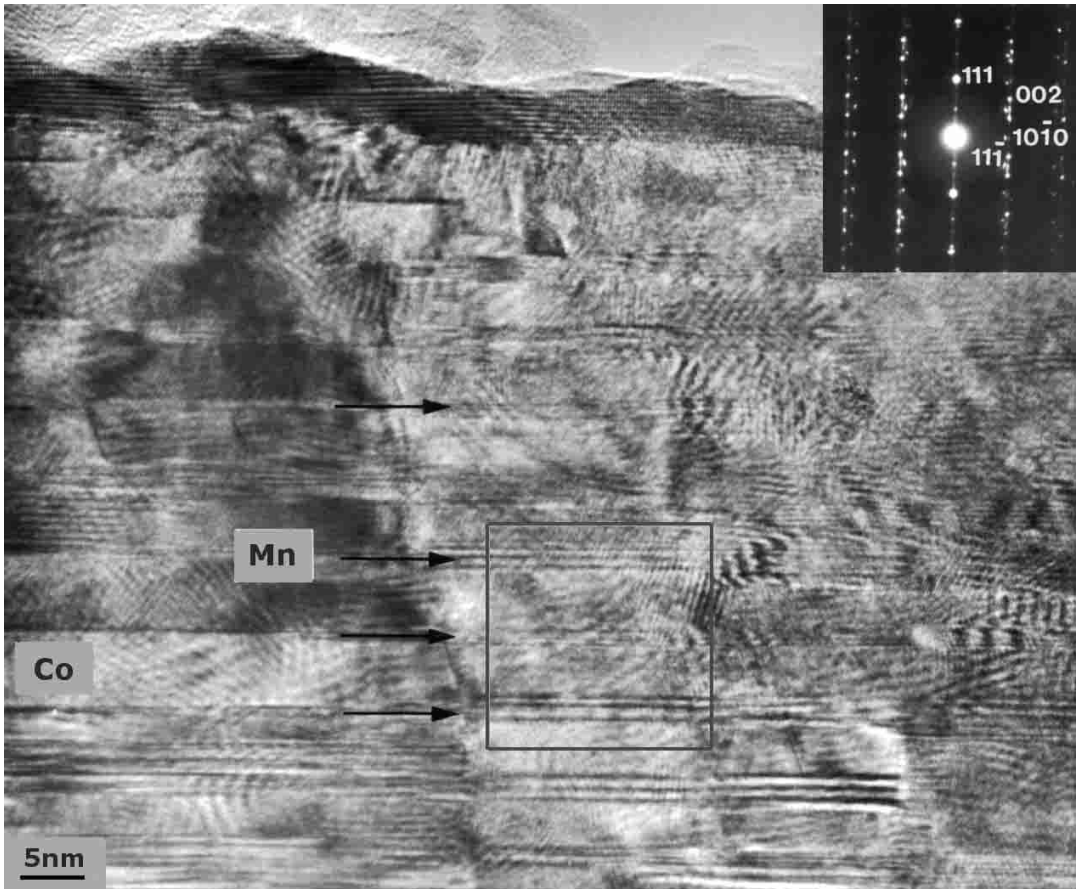

Fig. 14. Cross-section TEM image from the sample [Co 6 nm/Mn 0.4 nm]×12. The zone axis is $[11\bar{2}0]_{\mathrm{hcp}}$. The black arrows indicate the contrast related to the presence of the Mn layers. The corresponding SAED pattern is shown in the upper right corner. The area in the shown square was used for the image processing (see Fig. 15).

that are present in the growth direction at and around the manganese layers.

To retrieve precise information on the stacking of the layers and on the position of the defects present in the picture, the image was digitally processed. Fourier transform of a selected area provided a power spectrum corresponding to a diffraction pattern incorporating all the different peaks previously mentioned. An inverse Fourier transform using a mask to select the contribution from a chosen structure allows to image the area where this phase is present, an image comparable to a dark field electron image. The images presented in Figure 15 correspond to the inverse Fourier transform of the fcc $[11\bar{1}]$ and $[00\bar{2}]$ (Fig. 15c), the twin fcc $[11\bar{1}]$ (Fig. 15d) and the hcp $[10\bar{1}\bar{1}]$ (Fig. 15b). These digitally obtained images show clearly that the stacking in the centre of the cobalt layers is fcc and has only a few defects, whereas hcp Co or stacking faults appear in the assumed position of the Mn layers. Two points are worth mentioning regarding these images. First, it is difficult to derive whether the hcp Co phase is located below, above or around the Mn layer, and second, in some areas a continuity of the fcc phase can be observed throughout the assumed Mn layer.

5 Discussion and conclusions

The X-ray results show that the samples can be classified into two groups. For samples with thin Co layers, samples 1–3, the Co is mostly fcc. These can be described as having, in average, a stacking fault every 3 planes (medium α phase) and parts of perfect fcc crystal. For the thicker samples, two phases exist: an almost perfect fcc phase, and a highly faulted, though significantly less in quantity, hcp phase. The crystalline quality of the hcp part improves with increasing Co thickness ($\alpha \sim 0.85$).

The values of α obtained by NMR are closer to 0.5 (random stacking) than the values produced by X-rays. Nevertheless, taking into account the difference in probing of the two techniques, these values are in good agreement. Indeed, the X-ray spectra contain a contribution due to Mn and Co atoms at the interfaces, whereas for NMR, Mn and Co atoms are distinct. Additionally, the grain boundaries and the non-crystalline grains do not contribute to the X-ray spectra, while, for NMR spectra, they partly contribute.

From both techniques, when the Co thickness increases, one can derive the following tendencies: first, the density of stacking faults in the fcc part decreases,

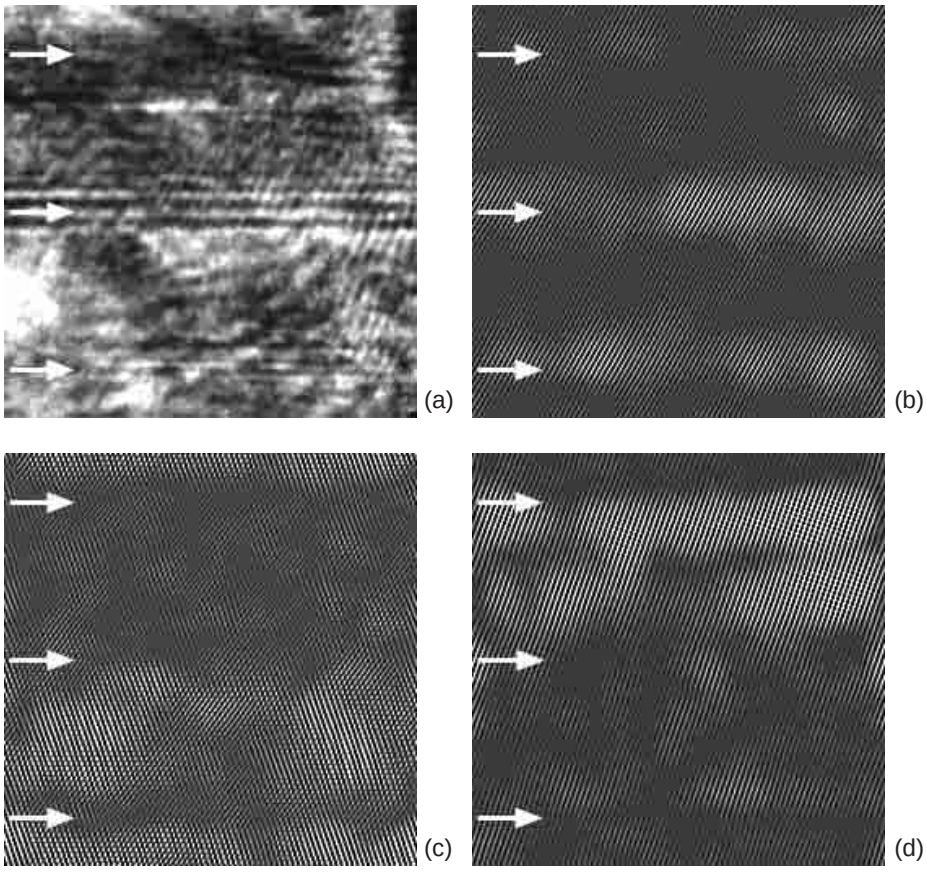

Fig. 15. Digitally processed images from the sample [Co 6 nm/Mn 0.4 nm]×12. (a) Section A from Figure 14. (b) Inverse FT using the $[10\bar{1}1]_{\mathrm{hcp}}$, hcp phase and stacking fault contribution. (c) Inverse FT using the $[11\bar{1}]_{\mathrm{fcc}}$, fcc phase contribution. (d) Inverse FT using the $[11\bar{1}]_{\mathrm{fcc\text{-}t}}$, twin fcc phase contribution.

and second, the hcp proportion increases but without a decrease in the density of stacking faults. During the growth, RHEED observations [21] have shown that the lattice parameter of Co progressively relaxes towards its bulk value when 7–8 monolayers are deposited. This limit represents the boundary between samples 3 and 4. Thus for samples 1–3, the Co layer is still strongly strained by the presence of Mn that has an extrapolated lattice parameter [21] of 0.2088 nm in the fcc phase (0.2035 nm for bulk cobalt). For samples 4–6, while the main part of the sample remains in the metastable fcc structure, the Co slowly, yet partially, relaxes towards its stable hcp bulk phase but still partially.

These results are in agreement with the TEM observations of sample 6 where strong strain contrast is visible. Image processing revealed that fcc and hcp stacking coexist in the sample, the hcp stacking is often found close to the Mn layer, while some fcc bridges exist through the very thin Mn layer. This is expected since, as shown by NMR, the Mn layer is actually spread over two atomic planes (discontinuous monolayer). These bridges also explain the large correlation length of the fcc stacking even for thin bilayers.

The observations allow to develop a model according to which the Co fcc phase is stabilised by the Mn, that acts as an fcc template due to a chemical and pseudomorphic mechanism. This is favourable due to the small energy difference between fcc and hcp structures [37]. Additional stabilisation mechanisms can be attributed either to the small strains that remain in the thicker samples or to a surfactant effect, when a small amount of Mn floats at the surface during the growth. Indications of such a surfactant effect have already been reported in the case of the growth of Ir/FeMn superlattices [38]. Moreover, manganese is known to stabilise the fcc phase of cobalt, as the martensitic transformation temperature strongly decreases with the Mn concentration [26]. The presence of Mn at the surface could induce the growth of fcc cobalt, even away from the Mn interface. This is confirmed experimentally by the fact that a Mn seed layer yields the fcc cobalt growth on Ru [21] (on which otherwise it grows as hcp).

The presence of the Mn at the surface could be related to a stable ordered alloy phase that would drive the Mn towards the surface during the subsequent deposition of the cobalt. A surface reconstruction has been observed recently on a fcc Co(001) surface [39]. On a sixfold symmetry surface $(111)_{\mathrm{fcc}}$, a large step in the in-plane lattice parameter when depositing the first Mn monolayer on Co [19,21] was also observed.

An additional explanation for the fcc cobalt growth could be found in the effect of the interface on the chemical potential of a stacking fault, as described by Redfield and Zangwill [40]. They demonstrate the possibility of having a chemical potential oscillating around the bulk value. Considering the small energy difference between the fcc and hcp phases of cobalt, this interfacial effect could be of prime importance.

Concluding, we believe that thin manganese layers stabilise the fcc cobalt phase as in the studied multilayers the cobalt is mostly fcc. Moreover, the perfection of the fcc stacking increases with the cobalt thickness and the stacking defects are mainly located at the position expected for the manganese layer. This apparent contradiction could be explained by assuming that the effect of the manganese presence on the cobalt growth is a surfactant and not a bulk effect.

Part of the TEM work has been performed within the framework of IUAP 4/10 of the Belgian government.

References

1. P. Grunberg, R. Schreiber, Y. Pang, M.B. Brodsky, H. Sowers, Phys. Rev. Lett. **57**, 2442 (1986).
2. J.J. Krebs, P. Lubitz, A. Chaiken, G.A. Prinz, Phys. Rev. Lett. **63**, 1645 (1989); *ibid.* J. Appl. Phys. **67**, 5920 (1990).
3. S.S.P. Parkin, N. More, K.P. Roche, Phys. Rev. Lett. **64**, 2304 (1990).
4. P. Bruno, C. Chappert, Phys. Rev. B **46**, 261 (1992).
5. E.E. Fullerton, D. Stoeffler, K. Ounadjela, B. Heinrich, Z. Celinski, J.A.C. Bland, Phys. Rev. B **51**, 6364 (1995).
6. S. Bouarab, H. Naitlaziz, M.A. Khan, C. Demangeat, H. Dreysse, M. Benakki, Phys. Rev. B **52**, 10127 (1995).
7. H. Dreysse, C. Demangeat, Surf. Sci. Rep. **28**, 67 (1997).
8. P. Kruger, O. Elmouhssine, C. Demangeat, J.C. Parlebas, Phys. Rev. B **54**, 6393 (1996).
9. M.N. Baibich, J.M. Broto, A. Fert, F. Nguyen Van Dau, F. Petroff, P. Etienne, G. Creuzet, A. Friederich, J. Chazelas, Phys. Rev. Lett. **61**, 2472 (1988).
10. S.S.P. Parkin, Phys. Rev. Lett. **71**, 1641 (1993).
11. D.M. Kelly, I.K. Schuller, V. Korenivski, K.V. Rao, K.K. Larsen, J. Bottiger, E.M. Gyorgy, R.B. van Dover, Phys. Rev. B **50**, 3481 (1994).
12. A. Dinia, S. Zoll, M. Gester, D. Stoeffler, J.P. Jay, K. Ounadjela, H.A.M. van der Berg, H. Rakoto, Eur. Phys. J. B **5**, 203 (1998).
13. Y. Henry, Ph.D. thesis, University Louis Pasteur, Strasbourg, 1995; Y. Henry, K. Ounadjela, Phys. Rev. Lett. **76**, 1944 (1996).
14. K. Uchiyama, I. Ishida, E. Hirota, K. Hamada, A. Okada, Jap. J. Appl. Phys. **36**, 114 (1997).
15. H.W. Zhao, M. Lu, Y.X. Sui, H.R. Zhai, D. Feng, Y. Chen, G.S. Dong, X.F. Jin, Appl. Phys. Lett. **70**, 2906 (1997).
16. M.E. Filipkowski, J.J. Krebs, G.A. Prinz, C.J. Gutierrez, Phys. Rev. Lett. **75**, 1847 (1995).
17. V. Chakarian, Y.U. Idzerda, H.J. Lin, C. Gutierrez, G.A. Prinz, G. Meigs, C.T. Chen, Phys. Rev. B **53**, 11313 (1996).
18. M.E. Filipkowski, C.J. Gutierrez, G.A. Prinz, J. Appl. Phys. **81**, 3785 (1997).
19. Y. Henry, V. Pierron-Bohnes, K. Ounadjela, J. Appl. Phys. **76**, 2817 (1994).
20. A. Michel, Ph.D. thesis, University Louis Pasteur, Strasbourg, 1995.
21. K. Ounadjela, P. Vennegues, Y. Henry, A. Michel, V. Pierron-Bohnes, J. Arabski, Phys. Rev. B **49**, 8561 (1994).
22. F. Gautier, D. Stoeffler, J. Magn. Magn. Mater. **93**, 10 (1991).
23. D. Muller, K . Ounadjela, P. Vennegues, V. Pierron-Bohnes, A. Arbaoui, J.P. Jay, A. Dinia, P. Panissod, J. Magn. Magn. Mater. **104**, 1873 (1992).
24. P. van der Sluis, J. Appl. Cryst. **27**, 1015 (1994).
25. M.S. Paterson, J. Appl. Phys. **8**, 805 (1952); A. Guinier, *Théorie et technique de la radiocristallographie* (Dunod, Paris, 1964); M.T. Sebastian, P. Krishna, Phys. Stat. Sol. **101**, 329 (1987).
26. K. Tsioplakis, T. Goedecke, Z. Metallk. **62**, 681 (1971).
27. W. Staiger, A. Michel, V. Pierron-Bohnes, N. Herrmann, M.C. Cadeville, J. Mat. Res. **12**, 161 (1997).
28. H.W. Zhao, Y. Chen, W.R. Zhu, G.S. Dong, X.F. Jin, M. Lu, H.R. Zhai, J. Appl. Phys. **81**, 2036 (1997).
29. P. Schieffer, C. Krembel, M.C. Hanf, D. Bolmont, G. Gewinner, J. Magn. Magn. Mater. **165**, 180 (1997).
30. E.A.M. van Alphen, S.G.E. de Velthuis, H.A.M. de Gronckel, K. Kopinga, W.J.M. de Jonge, Phys. Rev. B **49**, 17336 (1994).
31. J.F. Jauak, Phys. Rev. B **20**, 2206 (1979).
32. E.A.M. van Alphen, H.A.M. de Gronckel, P.J.H. Bloemen, A.S. van Steenbergen, W.J.M. de Jonge, J. Magn. Magn. Mater. **121**, 77 (1993).
33. C. Mény, E. Jedryka, P. Panissod, J. Phys. Cond. Matt. **5**, 1547 (1993).
34. P. Panissod, J.Ph. Jay, C. Mény, M. Wójcik, E. Jedryka, Hyperfine Int. **97-98**, 75 (1996).
35. C. Mény, P. Panissod, P. Humbert, J.P. Nozières, V.S. Speriosu, B.A. Gurney, R. Zehringer, J. Magn. Magn. Mater. **121**, 406 (1993).
36. C. Mény, P. Panissod, R. Loloee, Phys. Rev. B **45**, 12269 (1992).
37. A.M. Papon, J.P. Simon, P. Guyot, M.C. Desjonqueres, Phil. Mag. **39**, 301 (1979); Ericson, Acta Metall. **14**, 853 (1966).
38. H. Ardhuin, E. Snoeck, M.J. Casanove, H. Fischer, S. Andrieu, M. Piecuch, Thin Solid Films **318**, 189 (1998).
39. B.H. Choi, P.J. Bode, J.A.C. Bland, Phys. Rev. B **58**, 5166 (1998).
40. A.C. Redfield, A.M. Zangwill, Rapid Comm., Phys. Rev. B **34**, 1378 (1986).